# Inertio-Thermal Vapour Bubble Growth

Supplementary Information

**Patrick Sullivan[1]†, Duncan Dockar[1] Matthew K. Borg[1] Ryan Enright[2] and Rohit Pillai[1]**

[1]Institute for Multiscale Thermofluids, University of Edinburgh, Edinburgh, EH9 3FB, UK

[2]Thermal Management Research, $\eta$et department, Nokia Bell Labs, 600 Mountain Av., Murray Hill, 07974, NJ, USA

## S1. Generalised Rayleigh–Plesset Equation

The classical Rayleigh–Plesset equation for an incompressible liquid was generalised by Prosperetti (1982) to include non-Newtonian and mass transfer effects. In this case, the radial component of the momentum equation for an incompressible fluid in spherical coordinates is given as:

$$\rho_l \left( \frac{\partial u}{\partial t} + u \frac{\partial u}{\partial r} \right) = -\frac{\partial P}{\partial r} + \frac{1}{r^2} \frac{\partial}{\partial r} \left( r^2 \tau_{rr} \right) - \frac{\tau_{\theta\theta} + \tau_{\phi\phi}}{r}, \tag{S1.1}$$

where $\rho_l$ is the density of the liquid, $P$ and $u$ represent the pressure and velocity, respectively, at a radial distance $r$ and time $t$. $\tau_{rr}$, $\tau_{\theta\theta}$, and $\tau_{\phi\phi}$ represent the radial, polar and azimuthal elements of the viscous stress tensor, respectively. Given the identity $\tau_{\theta\theta} + \tau_{\phi\phi} = \tau_{rr}$ when assuming spherical symmetry (i.e. neglecting the $\theta$ and $\phi$ velocity components), this expression is integrated from the bubble radius $R$ to infinity giving:

$$R\dot{U}_l + 2\dot{R}U_l - \frac{1}{2}U_l^2 = \frac{1}{\rho_l} \left( P(R,t) - P_\infty - \tau_{rr}(R,t) + 3 \int_R^\infty r^{-1} \tau_{rr} dr \right), \tag{S1.2}$$

with $U_l$ representing the radial liquid velocity at the bubble interface, $P(R,t)$ the pressure on the liquid side of the interface, and $P_\infty$ the far field pressure.

The conditions of conservation of mass and momentum across the bubble interface give:

$$J = \rho_l \left( U_l - \dot{R} \right) = \rho_v \left( U_v - \dot{R} \right), \tag{S1.3}$$

$$J^2 \left( \frac{1}{\rho_v} - \frac{1}{\rho_l} \right) + P_v + P(R,t) + \tau_{rr}(R,t) = \frac{2\gamma}{R}, \tag{S1.4}$$

where $J$ is the mass flux across the interface, $P_v$, $\rho_v$ and $U_v$ the vapour pressure, density and velocity at the interface, respectively, and $\gamma$ is the surface tension.

Eliminating the $P(R,t)$ term, and expressing $\dot{R}$ in terms of $U_l$ and $J$, Prosperetti (1982) gives the generalised expression as:

$$R\dot{U}_l + \frac{3}{2}U_l^2 - \frac{J}{\rho_l} \left[ 2U_l + J \left( \frac{1}{\rho_v} - \frac{1}{\rho_l} \right) \right] = \frac{1}{\rho_l} \left( P_v - P_\infty - \frac{2\gamma}{R} + 3 \int_R^\infty r^{-1} \tau_{rr} dr \right). \tag{S1.5}$$

In the case of a Newtonian liquid, where $\tau_{rr} = 2\mu(\partial u/\partial r)$, this equation becomes:

$$R\dot{U}_l + \frac{3}{2}U_l^2 - \frac{J}{\rho_l} \left[ 2U_l + J \left( \frac{1}{\rho_v} - \frac{1}{\rho_l} \right) \right] = \frac{1}{\rho_l} \left( P_v - P_\infty - \frac{2\gamma}{R} - \frac{4\mu U_l}{R} \right). \tag{S1.6}$$

† Email address for correspondence: Patrick.Sullivan@ed.ac.uk

When the ratio of bubble to liquid density is low $\rho_v \ll \rho_l$, the effects of mass transfer can be neglected. This is the case when the fluid is away from the critical point. In this case, $J = 0$ and $U_l = \dot{R}$ and equation (S1.6) simplifies to the classical Rayleigh–Plesset equation (equation 2.2 of the paper).

## S2. Plesset–Zwick Equation

As a vapour bubble grows, heat must be extracted from the liquid to overcome the latent heat requirement for phase change to occur. The rate of heat transfer $\dot{Q}$ required to grow the bubble is given by:

$$\dot{Q} = \frac{4\pi}{3} h_{lv} \frac{d}{dt} \left( R^3 \rho_v \right), \tag{S2.1}$$

with $h_{lv}$ representing the latent heat of evaporation. This heat transfer rate must be matched by the heat conducted at the bubble interface:

$$\dot{Q} = -4\pi R^2 k \frac{\partial T}{\partial r}, \tag{S2.2}$$

where $k$ is the liquid thermal conductivity.

Plesset & Zwick (1954) provided a zero-order approximation for the bubble wall temperature:

$$T = T_\infty - \sqrt{\frac{\alpha}{\pi}} \int_0^t \frac{R^2(x)(\partial T/\partial r)_R}{\sqrt{\int_x^t R^4(y)dy}} dx, \tag{S2.3}$$

by assuming that heat is conducted through a thin thermal boundary layer, where $\alpha = k/\rho_l c_p$ is the thermal diffusivity of the liquid with $c_p$ representing the heat specific heat capacity at constant pressure, and $(\partial T/\partial r)_R$ is the temperature gradient at the bubble wall. Equating equations (S2.1) and (S2.2), and substituting the temperature gradient at the interface into equation (S2.3), an asymptotic solution for the bubble's radial velocity was derived:

$$\dot{R}_{\mathrm{PZ}} = Ja \sqrt{\frac{3\alpha}{\pi t}}, \tag{S2.4}$$

where the Jakob number $Ja$ is the ratio of sensible heat to latent heat, given by $Ja = \rho_l c_p \Delta T_0 / \rho_v h_{lv}$, where $\Delta T_0$ is the initial liquid superheat.

## S3. Complex Form of the FIT model

The *full inertio-thermal* (FIT) model for the radial velocity $\dot{R}$, is given by the root of the equation

$$\frac{2\sqrt{t}}{B} \dot{R}_{\mathrm{FIT}}^3 + \left( \frac{4A^2 t}{B^2} - 1 - \frac{\tau_{\mathrm{RP}}^2}{t^2} \right) \dot{R}_{\mathrm{FIT}}^2 - \frac{4A^2\sqrt{t}}{B} \dot{R}_{\mathrm{FIT}} + A^2 = 0, \tag{S3.1}$$

where $A$ and $\tau_{\mathrm{RP}}$ represent the inertial Rayleigh–Plesset limiting velocity and corresponding timescale, respectively, and $B = Ja\sqrt{12\alpha/\pi}$, as in the analysis of Mikic *et al.* (1970). In the case of $\tau_{\mathrm{RP}} = 0$, i.e. in the absence of dynamic inertial effects, the equation

can be factorised to give:

$$\underbrace{\left(\dot{R}-\frac{B}{2\sqrt{t}}\right)}_{\text{PZ}}\underbrace{\left(\dot{R}+A\left[\sqrt{\frac{A^2t}{B^2}+1}+\sqrt{\frac{A^2t}{B^2}}\right]\right)}_{\text{Rejected MRG}}\underbrace{\left(\dot{R}-A\left[\sqrt{\frac{A^2t}{B^2}+1}-\sqrt{\frac{A^2t}{B^2}}\right]\right)}_{\text{MRG}}=0. \tag{S3.2}$$

These roots correspond to the Plesset–Zwick (PZ) model, the rejected negative solution in the Mikic–Rohsenow–Griffith (MRG) analysis and the MRG model. This factorisation cannot be performed for finite $\tau_{\mathrm{RP}}$, however, the equation can be solved using Cardano's formula for solving cubic equations in the form $ax^3+bx^2+cx+d=0$. For this analysis, it becomes convenient to define the following terms:

$$\Delta_0 = b^2-3ac, \tag{S3.3}$$

$$\Delta_1 = 2b^3-9abc+27a^2d, \tag{S3.4}$$

$$C=\sqrt[3]{\frac{\Delta_1\pm\sqrt{\Delta_1^2-4\Delta_0^3}}{2}}. \tag{S3.5}$$

The discriminant of the equation can then by given by $\Delta=(4\Delta_0^3-\Delta_1^2)/27a^2$. Substituting the values of $a$, $b$, $c$, and $d$ from equation (S3.1) and rearranging we can write the discriminant as:

$$\Delta=A^2\left(A^2\frac{80t}{B^2}\chi+A^2\frac{4t}{B^2}+12\chi^2+12\chi+4+4\chi\left(A^2\frac{4t}{B^2}-\chi\right)^2\right)>0, \tag{S3.6}$$

where $\chi$ is the ratio $\tau_{\mathrm{RP}}^2/t^2$. As all of the terms in equation (S3.6) are positive, the discriminant will always be positive. This indicates that the equation will have three distinct real solutions, except at $t=0$, where two of the solutions will be identical ($\dot{R}=0$).

The FIT model can then be expressed in the form:

$$\dot{R}=-\frac{1}{3a}\left(b+\xi^nC+\frac{\Delta_0}{\xi^nC}\right), \tag{S3.7}$$

with $\xi$ being the principal cube root of unity:

$$\xi=\frac{-1+\sqrt{3}i}{2}, \tag{S3.8}$$

and $n$ being 2. This corresponds to the canonical third of the three cube roots being the FIT model. As in the case with no dynamic inertial effects (equation (S3.2)), the first canonical root corresponds to the PZ model and the second to the rejected solution from the MRG analysis. While we have shown that the roots of the equation are real, it is not possible to express the roots in a real form. The roots of this type of cubic equation can only be written symbolically in a complex form. However, when the numeric value of the roots are calculated, they will always be real.

## S4. Agreement of IT Models

The approximations made in the derivations of the *approximate inertio-thermal* (AIT) and *simple inertio-thermal* (SIT) models introduce additional errors into the predictions when compared to the FIT model. Analysing the disagreement between the model predictions gives further insight into the applicability of these models. Figure S1 shows

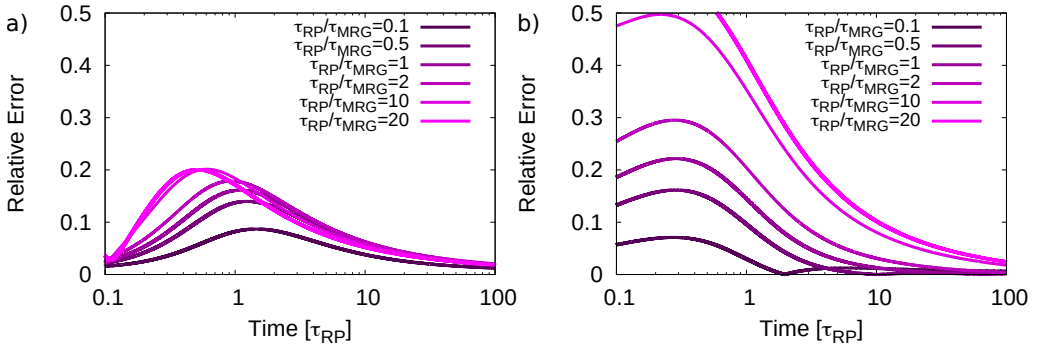


FIGURE S1. Relative error of the (a) AIT and (b) SIT models compared to the FIT model for various ratios of $\tau_{\mathrm{RP}}/\tau_{\mathrm{MRG}}$.

plots of the relative error of the (a) AIT and (b) SIT models to those predicted by the FIT model. These error values are given for a bubble of initial radius $R_0$ as:

$$\text{Relative Error} = \frac{|R - R_{\mathrm{FIT}}|}{R_{\mathrm{FIT}} - R_0}. \tag{S4.1}$$

To evaluate model agreement, the radii predicted by the AIT model were compared to those values predicted by the FIT model for various values of the ratio $I = \tau_{\mathrm{RP}}/\tau_{\mathrm{MRG}}$. The relative error in the AIT predictions is presented in figure S1(a), which shows that the error peaks at $t \approx \tau_{\mathrm{RP}}$ for $\tau_{\mathrm{RP}}/\tau_{\mathrm{MRG}} = 1$, moving to earlier times as this ratio increases and later as it decreases. This maximum relative error value is shown to be $\sim 20\%$ across all values of $I$, dropping quickly beyond that and reaching a value of $\sim 5\%$ after 10 inertial timescales. The maximum relative error is obtained for a ratio of $I \approx 4$, with the error decreasing as the ratio is changed from this value.

The SIT model predictions are compared to the FIT model in figure S1(b) to highlight when it is appropriate to use the model. The relative error now peaks consistently at a time of $0.25\tau_{RP}$. We can see that there is improved agreement compared to the AIT model for ratios $\tau_{\mathrm{RP}}/\tau_{\mathrm{MRG}} < 1$, as the relative error of the SIT model goes to zero at comparatively lower values of $\tau_{RP}$, in contrast with the AIT model in figure S1(a), where they remain non-zero for the entire duration. The maximum error increases with $\tau_{\mathrm{RP}}/\tau_{\mathrm{MRG}}$ and, unlike the AIT model, continues to increase indefinitely with $\tau_{\mathrm{RP}}/\tau_{\mathrm{MRG}}$.

In the paper, the FIT, AIT, and SIT models are given in terms of the variables $A$, $B$, and $\tau_{\mathrm{RP}}$. As these equations are dependant on three variables, investigating their influence on the relative error is important. It then becomes convenient to analyse the equations in terms of three alternate variables, namely $\tau_{\mathrm{RP}}$, $\tau_{\mathrm{MRG}}$ and $R_0$. In this case, we can clearly see that for a given ratio of $\tau_{\mathrm{RP}}/\tau_{\mathrm{MRG}}$ the values are dependant only on $R_0$. Therefore we have shown in figure S2 the variation of the errors plotted in figure S1 for various values of $R_0$ for the case of $\tau_{\mathrm{RP}}/\tau_{\mathrm{MRG}} = 1$. We have presented these radii in terms of $\tau_{\mathrm{RP}}$ with a $1\,m/s$ scaling. We can see that there is excellent agreement in the error values for both the AIT and SIT equations across all values of $R_0$, indicating that the error is dependant only on the ratio of the inertial and thermal timescales $\tau_{\mathrm{RP}}/\tau_{\mathrm{MRG}}$.

## S5. Effect of Temperature-Pressure Relationship

One of the most significant sources of error in the MRG model is the simplification of the temperature-pressure relationship of the fluid (Lee & Merte 1996; Robinson & Judd

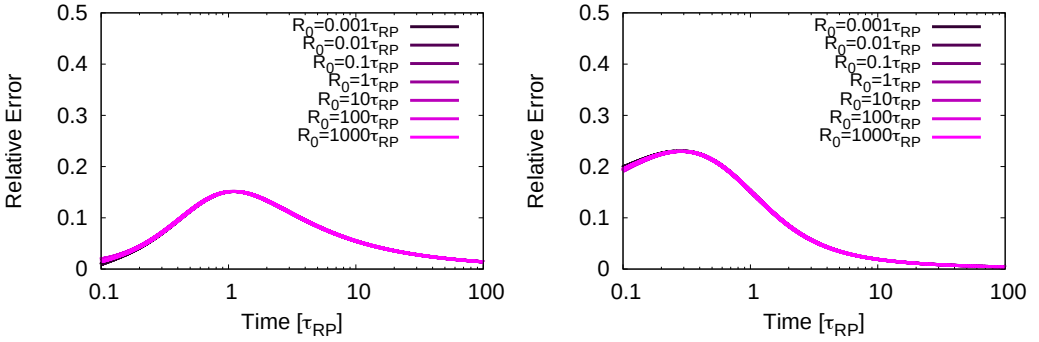


FIGURE S2. Relative error of the (a) AIT and (b) SIT models compared to the FIT model for various initial radii at a timescale ratio of $\tau_{\mathrm{RP}}/\tau_{\mathrm{MRG}} = 1$.

2004; Prosperetti & Plesset 1978). In their original work, Mikic *et al.* (1970) approximated this relationship using the integrated Clapeyron equation:

$$P_v - P_\infty = \frac{\rho_v h_{lv}}{T_{\mathrm{sat}}} \left| T_v - T_{\mathrm{sat}} \right| . \tag{S5.1}$$

This relationship accurately captures the slope of the temperature-pressure curve near the saturation temperature but consistently underestimates the actual vapour pressure (Theofanous & Patel 1976; Prosperetti & Plesset 1978). This leads to under-predictions of bubble radii as the inertial limiting velocity is under-predicted. This is particularly noticeable in the inertial-controlled regime, i.e. for $t < \tau_{\mathrm{MRG}}$. Lee & Merte (1996) compared the predictions of the model to their numerical calculations using a more accurate temperature-pressure relationship. They showed that the MRG model consistently under-predicted the radius, with a maximum error of 40%.

To more accurately capture the inertial limiting velocity, a linear relationship between the fluid temperature $T_v$ and vapour pressure, in terms of the initial pressure difference $\Delta P_0$, has been used instead (Prosperetti & Plesset 1978; Robinson & Judd 2004):

$$\frac{T_v - T_{\mathrm{sat}}}{\Delta T_0} = \frac{P_{\mathrm{v}} - P_\infty}{\Delta P_0}. \tag{S5.2}$$

This linear relationship accurately captures the inertial limiting velocity. However, the vapour pressure is overestimated as the bubble grows and cools, resulting in over-predictions of the bubble radius. In their comparisons of the MRG model using this linear temperature-pressure relationship, Lee & Merte (1996) showed that the bubble radii were always over-predicted, again with a maximum error of 40%.

A surprising result in the results presented in the paper is the apparent improved agreement of the SIT model with the cases tested compared to the AIT model, which is counter-intuitive given the AIT model captures more physics and is therefore expected to be more accurate. We explain this result in a straightforward way using two facts: a) the IT models rely on equation (S5.2) to model the temperature-pressure relationship, which means that they are expected to overpredict the bubble radii as discussed previously; and b) the SIT model assumes that cooling is occurring as if the bubble is growing at its inertial limiting velocity and subsequently increases the rate at which bubble growth slows in the early stages†. Therefore, as per a) above, both AIT and SIT overpredict the

† It is for this reason, as we have shown in the derivation of the model, that it should only be applied when the inertial timescale $\tau_{\mathrm{RP}}$ is greater than the thermal timescale $\tau_{\mathrm{MRG}}$.

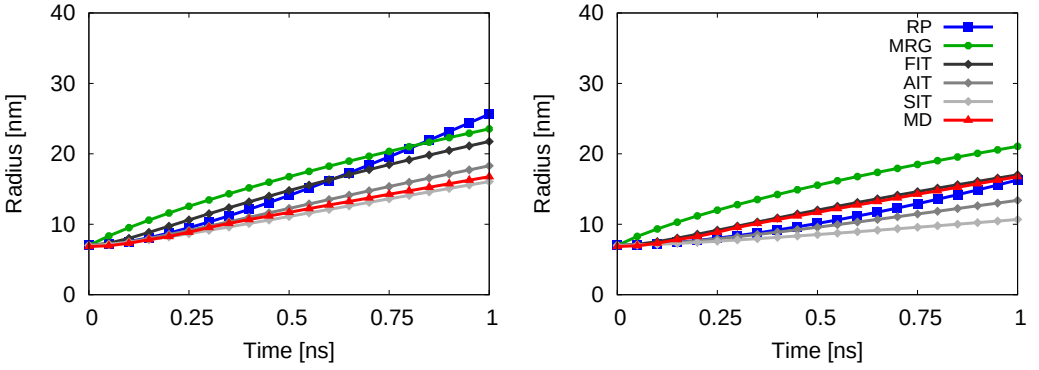


FIGURE S3. Predictions of the RP, MRG, and IT models compared to MD data using (a) the Clapeyron equation (S5.1) and (b) the linear relationship (equation (S5.2)) as the temperature-pressure relationship.

bubble radius, but b) means the SIT model consistently underpredicts the bubble radius relative to AIT. The "fortuitous self-cancellation" that results from a) and b) is that SIT deceptively appears to give more accurate predictions in the paper figures, but this only results from a systematic (i.e., not physics-based) underestimation of the bubble radius which happens to "reduce" the overall error in this instance.

When the Clapeyron equation is used, we see an under-prediction of the radius by both the AIT and SIT models. This is expected, as equation (S5.1) under-predicts the initial vapour pressure. This can be further seen by comparing against the entirely inertial Rayleigh–Plesset equation, which under-predicts the bubble size. In this case, the error of the AIT model increases to 40%, matching the maximum errors seen in the MRG model, while the SIT model error increases to 60% as the inherent error in the model and the error in the temperature-pressure relationship compound. Interestingly, we see excellent agreement of the FIT equation, which does not capture the effects of capillarity and viscosity. The FIT model's over-predictions due to the absence of capillarity and viscosity appear to be compensated by the under-predictions of the temperature-pressure relationship.

## S6. Molecular Dynamics Simulation Methodology

Molecular dynamics (MD) simulations were performed to measure the growth of nanoscale vapour bubbles using the open source software LAMMPS (Plimpton 1995). The interactions between the molecules were calculated using the truncated Lennard–Jones potential:

$$U(r_{ij}) = 4\epsilon_{ij}\left[\left(\frac{\sigma_{ij}}{r_{ij}}\right)^{12} - \left(\frac{\sigma_{ij}}{r_{ij}}\right)^{6}\right], \tag{S6.1}$$

where $\sigma$ is the characteristic length scale, $\epsilon$ is the potential well depth, and $r$ is the distance between two molecules, denoted by the subscripts $i$ and $j$. The interaction parameters used in these simulations are $\sigma = 0.34$ nm and $\epsilon = 0.2392$ kcal/mol, respectively, which were chosen to model Argon (Maroo & Chung 2008). The potential is truncated for values of $r > r_{\text{cut}}$, where $r_{\text{cut}} = 1.3$ nm. The simulations are performed with a timestep of 5 fs.

The system setup used in the MD simulation is shown in Figure S4(a). A liquid cube of side length 60 nm was created using the software package Packmol (Martínez *et al.* 2009).

The number of argon molecules $N$ was chosen to be slightly lower than the saturation density, creating a supersaturated liquid. For the 130 K simulations a value of $N \approx 3.7 \times 10^6$ argon molecules were used. In the higher temperature ($T = 135\,\mathrm{K}$) simulations, a lower value of $N \approx 3.2 \times 10^6$ was used, reflecting the lower saturation density. This fluid slab was contained between two FCC walls, which are used to maintain the fluid pressure during the bubble's growth. During the simulation, one wall is kept fixed in place, while the second is allowed to translate in the normal direction after fluid equilibration.

The system is initially equilibrated (with both surfaces fixed) in the NVT ensemble until the potential energy of the system reached a steady value. The piston is then released to apply the required pressure $P_\infty$, through a constant force $F$, applied to each particle. The force is given by $F = P_\infty A_P / N_P$, where $A_P$ is the wetted area of the piston, and $N_P$ is the number of piston atoms. During this stage, a fictitious damping force was also added to the piston to prevent excessive oscillations, which could lead to cavitation bubbles forming in the liquid. The damping force was calculated by scaling the velocity of the piston by a damping constant, $c$. The critical damping constant can be calculated as $c = 2\sqrt{mK}$, using the mass of the piston $m$, and the stiffness of the fluid $K$, which was measured by adjusting the pressure of the piston in separate equilibrium simulations. The system was equilibrated again in the NVT ensemble until the piston reached a steady position, at which point the damping was removed from the piston.

At this point in the simulation setup, molecules were removed from a spherical region in the liquid. A smaller number of vapour molecules were then inserted into this void, with the number of molecules set to match the saturated vapour density, as highlighted by the simulation segment in Figure S4(b). This system was then run in the NVT ensemble for 1000 timesteps to equilibrate the bubble, preventing any cavitation bubbles from forming in the system, and the setup was fully equilibrated at this point. The production simulations could then be performed in the NVE ensemble. These simulations were run for a total of 200,000 timesteps.

In the cases tested here, the bubbles were large enough that thermal noise in the measurement of thermodynamic properties, such as temperature or pressure, did not play a significant role in determining the dynamics of the bubbles (Allen & Tildesley 2017, pp. 46-49). It is worth noting that thermal noise may make it more difficult to produce accurate measurements for smaller bubbles.

## S7. Bubble Volume Measurements

The radius of the bubble was determined by measuring the volume of the bubble, $V$, and converting it to an equivalent radius $R_{\mathrm{eq}}$ using the equation $R_{\mathrm{eq}} = (3V/4\pi)^{1/3}$. The volume of the bubble was measured by overlaying the simulation domain with a cubic lattice of nodes prior to running the simulation, and determining the number of these nodes in vapour-like regions. A node was determined to be in liquid-like or vapour-like regions based on its coordination number, which is defined as the number of molecules within a specified distance. A cutoff of 15 argon molecules within a distance of 1.3 nm was chosen as the criterion for a vapour-like lattice node. This criterion was determined from analysing the radial distribution function of the liquid and vapour in a separate simulation, and focusing on a coordination number clearly between the values of liquid and vapour. Each lattice node determines whether a cube of volume $d^3$, where $d$ is the spacing of the lattice nodes, is in a liquid-like or vapour-like region. The total bubble volume is therefore the number of vapour-like lattice nodes multiplied by $d^3$. An example of the vapour like lattice nodes can be seen in Figure S4(c). This bubble measurement

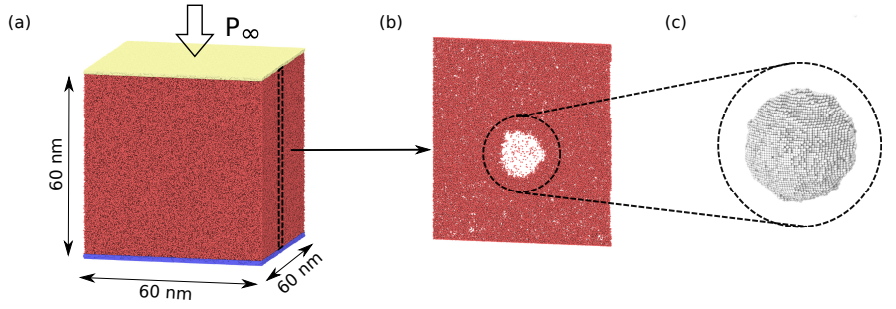


FIGURE S4. (a) The MD simulation domain, red atoms show argon, blue atoms show the bottom (stationary) surface and yellow atoms show the piston. (b) A simulation slice, showing the presence of a vapour bubble in the bulk of the fluid. (c) Detected bubble from lattice coordination number showing vapour like nodes.

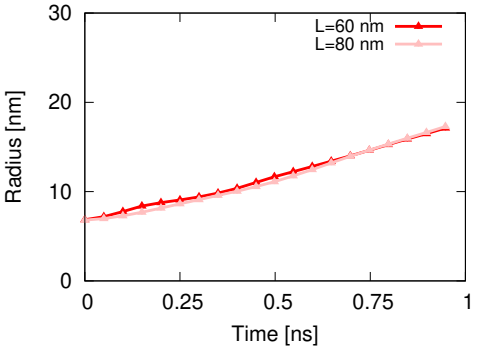


FIGURE S5. The measured radius of a vapour bubble for domain sizes of 60 nm and 80 nm with $T = 130\,\mathrm{K}$, $P = 0.1\,\mathrm{MPa}$, and $R_0 = 7\,\mathrm{nm}$.

technique can be implemented directly in LAMMPS by creating fictitious molecules to represent the lattice nodes.

To show the independence of the measured bubble radii from the size of the domain, secondary simulations were performed with a side length of 80 nm. As before, the system was equilibrated prior to the insertion of a bubble and then allowed to grow in the NVE ensemble. Figure S5 shows a comparison of the growth rates measured for the case of $T = 130\mathrm{K}$, $P = 0.1\mathrm{MPa}$, and $R_0 = 7\mathrm{nm}$ for the two domain sizes: 60 nm and 80 nm. From the plot we can see good agreement between the two data sets. This is to be expected as the sum of the bubble radius and diffusive thermal length scale, given as $\delta = \sqrt{\alpha t}$, is less than the distance between the bubble interface to the periodic boundary throughout the simulation.

## REFERENCES

ALLEN, MICHAEL P. & TILDESLEY, DOMINIC J. 2017 *Computer simulation of liquids: Second edition*, 2nd edn. Oxford University Press.

LEE, H. S. & MERTE, H. 1996 Spherical vapor bubble growth in uniformly superheated liquids. *Int. J. of Heat and Mass Transfer* **39** (12), 2427–2447.

MAROO, S. C. & CHUNG, J. N. 2008 Molecular dynamic simulation of platinum heater and associated nano-scale liquid argon film evaporation and colloidal adsorption characteristics. *J. Colloid Interface Sci.* **328** (1), 134–146.

MARTÍNEZ, L., ANDRADE, R., BIRGIN, E. G. & MARTÍNEZ, J. M. 2009 Packmol: A Package

for Building Initial Configurations for Molecular Dynamics Simulations. *J. Comp. Chem.* **30** (13), 2157–2164.

Mikic, B. B., Rohsenow, W. M. & Griffith, P. 1970 On bubble growth rates. *Int. J. of Heat and Mass Transfer* **13** (4), 657–666.

Plesset, M. S. & Zwick, S. A. 1954 The growth of vapor bubbles in superheated liquids. *J. Appl. Phys.* **25** (4), 493–500.

Plimpton, S. 1995 Fast Parallel Algorithms for Short-Range Molecular Dynamics. *J. Comp. Phys.* **117**, 1–19.

Prosperetti, A. 1982 A generalization of the Rayleigh-Plesset equation of bubble dynamics. *Phys. Fluids* **25**, 409.

Prosperetti, A. & Plesset, M. S. 1978 Vapour-bubble growth in a superheated liquid. *J. Fluid Mech.* **85** (2), 349–368.

Robinson, A. J. & Judd, R. L. 2004 The dynamics of spherical bubble growth. *Int. J. of Heat and Mass Transfer* .

Theofanous, T. G. & Patel, P. D. 1976 Universal relations for bubble growth. *Int. J. of Heat and Mass Transfer* **19** (4), 425–429.